communications materials

A Nature Portfolio journal

Article

https://doi.org/10.1038/s43246-025-01071-z

Graphene-enhanced perovskite hybrid photodetectors with ultra-sensitivity and stability via inkjet printing

Junaid Khan[1] ✉, Júlia Marí-Guaita[1], Joshua D. Forero[1], Kenneth Lobo[1], Giovanni Vescio[1], Francisco Palacio[1], Carina Pareja-Rivera[2], Martin Weis[3], Raúl I. Sánchez[4], Juan P. Martínez[4], Iván Mora-Seró[2], Sergi Hernández[1], Albert Cirera[1] & Blas Garrido[1]

Metal-halide perovskites are promising materials for optoelectronic applications due to their strong light absorption, tunable bandgaps, and solution-processability. However, their use in photodetectors is often limited by low carrier mobility and degradation over time as compared to advanced 2D nanomaterials. Here, we report ultrasensitive photodetectors based on inkjet-printed nanocrystalline films of mixed-phase raisin bread $CsPbBr_3/Cs_4PbBr_6$ perovskite integrated on graphene platforms. The combination of a photoconductive mixed-phase perovskite and a high-mobility 2D graphene channel enables efficient photogating and broadband charge transport. This device architecture achieves exceptional performance with responsivities surpassing 5.7×10^4 A W^{-1} and detectivities exceeding 10^{16} Jones at 312 nm. The enhanced performance arises from the synergistic interplay between charge confinement in the perovskite domains and ultrafast carrier extraction by graphene. Moreover, the fabricated photodetectors exhibit remarkable operational stability, a longevity primarily attributed to the unique composite raisin-bread architecture of the inkjet-printed perovskite films. This work offers a scalable and sustainable strategy for high-performance broadband photodetection.

Photodetectors (PDs) are pivotal components in modern optoelectronic systems, serving as the bridge between optical and electrical domains[1]. These devices function by converting incident light ranging from ultraviolet to near-infrared wavelengths into measurable electrical signals, enabling a wide array of technologies, such as fast detection, high sensitivity and broad spectral coverage[2,3]. Their versatility makes them indispensable in numerous sectors, including medical diagnostics, biological and chemical sensing, environmental monitoring, optical communication systems, night vision, missile-launch warning systems, digital imaging and industrial automation[3–7]. The performance of PDs is generally evaluated based on key parameters, such as responsivity, detectivity, response time, linear dynamic range, and noise equivalent power (NEP). Enhancing these characteristics while ensuring scalability, flexibility, and cost-efficiency remains a central challenge in the development of next-generation PDs.

To meet these demanding criteria, researchers have increasingly turned to novel semiconducting materials and innovative fabrication techniques that offer tunability, high efficiency, and compatibility with modern manufacturing trends[8]. In recent years, halide perovskites have emerged as one of the most promising classes of semiconducting materials for optoelectronic applications[9–15]. Their unique combination of favorable properties, such as tunable direct bandgaps, high optical absorption coefficients, long carrier diffusion length, low trap-state densities, high photoluminescence quantum yields (PLQYs) and small exciton binding energy, makes them particularly attractive for light detection technologies[16–18]. Specifically, the all-inorganic cesium lead bromide perovskite ($CsPbBr_3$) has garnered significant attention due to its enhanced ambient and thermal stability compared to its organic-inorganic hybrid counterparts, as well as its efficient photon-to-electron conversion[19]. Its optoelectronic tunability also allows for selective detection across specific spectral ranges, making it ideal for broadband and narrowband photodetector designs[20].

The evolution of fabrication methodologies, particularly printed technologies, complements these material innovations by enabling scalable, ecofriendly, and cost-efficient production[21,22]. Among various emerging printing techniques, inkjet printing stands out due to its additive, non-contact nature, digital patterning capabilities, and minimal material waste[23,24]. This technique allows for the precise deposition of functional inks

[1]MIND-IN2UB, Department of Electronics and Biomedical Engineering, University of Barcelona, Barcelona, Spain. [2]Institute of Advanced Materials (INAM), Universitat Jaume I, Castelló de la Plana, Spain. [3]Institute of Electronics and Photonics, Slovak University of Technology, Bratislava, Slovakia. [4]Instituto de Ciencia de los Materiales, Universidad de Valencia, Valencia, Spain. ✉e-mail: junaidkhan@ub.edu

onto diverse substrates, including paper, plastic, textiles, and biodegradable films, without the need for masks, vacuum systems, or hazardous chemicals, contributing to the goal of green electronic manufacturing[25]. Inkjet printing enables low-temperature processing, making it suitable for flexible and sensitive substrates, and facilitates the integration of complex, multi-material heterostructures through layer-by-layer deposition, suitable for various applications, including PDs for wearable health monitoring, implantable optoelectronics, and artificial vision systems[26–29].

The performance of PDs, particularly their external responsivity, is strongly influenced by the photoconductive gain, which plays a crucial role in photoconductors and can be described by Eq. (1). In this expression, "τ_{life}" represents the carrier lifetime, which is the average duration that photo-generated charge carriers exist before recombining. The symbol "q" denotes the elementary charge, while "μ" stands for carrier mobility, which quantifies how quickly carriers move through the semiconductor material under an electric field. "V_{ds}" is the drain-source voltage applied across the device, and L is the channel length between the electrodes. From this relationship, it is evident that maximizing the carrier mobility μ plays a critical role in enhancing the responsivity of PDs, as it directly contributes to the amplification of the photocurrent especially in devices operating based on photoconductive mechanism.

$$R_{ext} = \frac{I_p}{P_{in}} \frac{\tau_{life} \mu V_{ds}}{L^2} \quad (1)$$

Where R_{ext} = External responsivity (A/W), I_p = Photocurrent (A), i.e., the current generated due to light exposure, P_{in} = Incident optical power on the active area of the device (W), τ_{life} is the carrier lifetime,μ is the charge carrier mobility, V_{ds} is the source-drain bias voltage, L is the channel length, and $\frac{\tau_{life}\mu V_{ds}}{L^2}$ also known as gain.

$CsPbBr_3$ nanocrystals (NCs) are promising photoactive materials for PDs due to their excellent light-harvesting capabilities. However, a key limitation of these perovskite (PVK)-based PDs is their relatively low intrinsic charge carrier mobility in the range of 1–5 $cm^2 V^{-1} s^{-1}$ for thin films NCs due to grain boundaries, traps and surface defects, whereas in single crystal perovskites it could go up to a maximum of 60 $cm^2 V^{-1} s^{-1}$. This restricts photoconductive gain and, consequently, limits the external responsivity[30,31]. In contrast, graphene, a two-dimensional, sp^2-hybridized carbon material, exhibits extraordinary electrical properties, with carrier mobilities reaching up to ~40,000 $cm^2 V^{-1} s^{-1}$, which is essential for rapid carrier extraction. Despite its high charge transport performance, graphene's light absorption is limited to only ~2.6%, rendering it unsuitable as a standalone photoactive material for photodetection applications[32–35]. Nevertheless, its ultrafast carrier mobility and efficient charge transport characteristics make it an ideal partner to complement the strong light absorption of perovskite materials in hybrid photodetector architectures[36]. By combining perovskites with single-layer graphene (SLG) or graphene derivatives, one can overcome the mobility limitations of perovskites. This hybridization not only facilitates efficient charge extraction but also suppresses carrier recombination, thereby significantly enhancing both gain and responsivity.

To harness the unique properties of SLG and PVK, numerous studies have focused on fabricating hybrid heterostructures combining these two materials, as summarized in Table 1. For instance, Akhavan et al.[27], developed a fiber-based photodetector using a triple-cation mixed-halide perovskite as the photoactive layer, with SLG serving as a rapid charge transport channel. Similarly, Malik et al.[37], fabricated a paper-based photodetector by first depositing SLG using spray lithography, followed by spray-coating of $CsPbBr_3$. In another study, Lee et al.[38], utilized a Si/SiO_2 substrate to construct a photodetector incorporating CVD-grown SLG and $CH_3NH_3PbI_3$. Sun et al.[39] extended the application of the SLG/perovskite hybrid heterostructure into the field of biosensing, while Zhu et al.[40], demonstrated improved solar cell performance by integrating graphene quantum dots as an electron transport layer between the perovskite and TiO_2.

These studies indicate the significant potential of SLG/PVK hybrid heterostructures for diverse optoelectronic applications. However, current fabrication techniques often involve complex processing steps, high-temperature treatments, and limited substrate compatibility, hindering their scalability and integration into flexible or wearable systems. Additionally, although $CsPbBr_3$ perovskite is valued for its excellent optoelectronic properties, it suffers from poor environmental stability and a narrow absorption range, which restrict its effectiveness for broadband photodetection and long-term device operation[41].

In our previous work[42], we demonstrated that mixed-phase perovskite films can be synthesized from $CsPbBr_3$ inks by simply adjusting the annealing temperature after inkjet printing. This straightforward approach results in the formation of $CsPbBr_3$ NCs embedded in Cs_4PbBr_6 matrices like a raisin bread structure, effectively enhancing the material's environmental robustness by reducing ion migration and moisture sensitivity. Additionally, this structure broadens the optical absorption range, particularly in the UV region, rendering the material highly suitable for broadband photodetection. Building on this advancement, we report the fabrication of SLG/PVK PDs entirely via a facile, low-cost, and environmentally friendly inkjet printing process, implemented on CVD-grown SLG platforms.

Remarkably, the devices operate without any external gating, yet achieve a responsivity exceeding 57,000 A/W at 312 nm under a 5 V bias placing them among the highest-performing broadband PDs fabricated via such a facile process. They exhibit a broad spectral response from 270 to 650 nm, excellent repeatability across multiple on/off cycles, and long-term operational stability in ambient conditions for over 6 months. Importantly, the use of mask-less, vacuum-free inkjet printing enables single-step deposition of the perovskite layer directly onto the SLG platform. This fabrication strategy not only ensures compatibility with flexible substrates but also aligns with roll-to-roll processing ambitions, highlighting the potential for scalable, cost-effective manufacturing of next-generation optoelectronic systems for wearable, artificial vision, and environmental sensing applications.

Results and discussion

Fabrication and characterization hybrid graphene/perovskite photodetector

Graphene/perovskite (PVK-G) hybrid photodetector was fabricated on commercially available FETS20 chip in which perovskite absorbs light and

Table 1 | Summary of hybrid graphene perovskite heterostructure devices and their applications

Sr. No	Substrate	Materials	Fabrication method	Application	Reference
1	Silica fibers	SLG/mixed halide perovskite	CVD, wet transfer and spin coating	Fiber photodetector	27
2	Silica fibers	MLG/$CsPbBr_3$	Dip coating and drop casting	Fiber photodetector	28
3	Paper	SLG/$CsPbBr_3$	Spray lithography and spray coating	Sustainable photodetector	37
4	Si/SiO_2	SLG/$CH_3NH_3PbI_3$	CVD and spin casting	Photodetector	38
5	Si/SiO_2	SLG/$CsPbI_3$ PQDs	CVD, wet transfer and spin coating	Cytokine biosensor	39
6	Glass	$CH_3NH_3PbI_3$/GQD/TiO_2	Electrochemical method	Solar cells	40

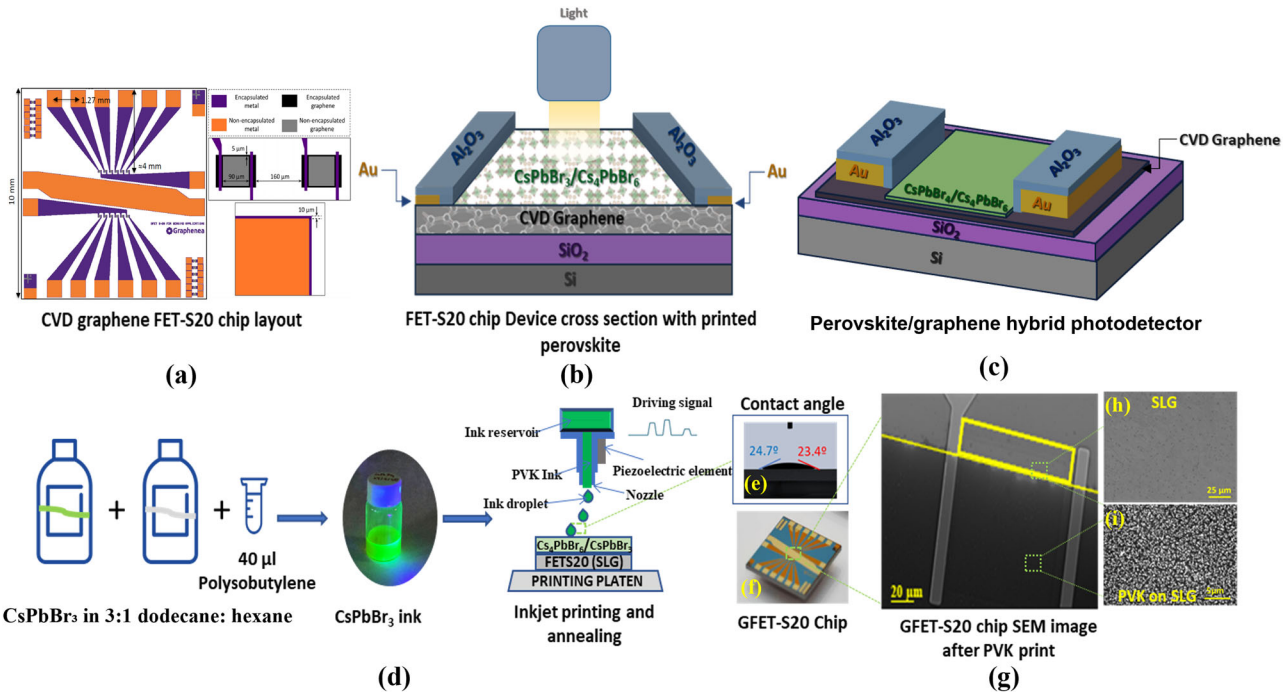

Fig. 1 | Fabrication and structural characterization of the perovskite–graphene field-effect transistor (GFET) array. a Schematic layout of the graphene field-effect transistor (GFET) array structure. **b**, **c** Cross-sectional and perspective illustrations of the device architecture showing the CVD graphene layer on Si/SiO_2, overlaid with inkjet-printed $CsPbBr_3/Cs_4PbBr_6$ perovskite layer **d** perovskite ink preparation, printing and annealing process. **e** Optical contact angle image of the printed film showing good wettability on the substrate. **f** Digital picture of printed GFET substrate **g** low resolution SEM image highlighting the printed perovskite layer on SLG. **h**, **i** High- resolution SEM images of CVD graphene and perovskite layers on the FETS20 platform.

generate electron–hole pairs, and graphene acts as a fast carrier transport layer. The device layout of the FETS20 chip is given in Fig. 1a, which consist of 6 square blocks per side each measuring 90 µm of SLG connected via a gold electrode (source and drain) with an insulating layer of Al_2O_3. The device cross-section after perovskite deposition is represented in Fig. 1b illustrating substrate, SLG as transport layer and perovskite as absorption layers along with Au contacts and insulating layers, whereas the device schematic is given in Fig. 1c. The schematic of the entire inkjet printed fabrication process of the hybrid PVK-G photodetector is illustrated in Fig. 1d. The inkjet printing process was optimized based on our previous studies[42], where we demonstrated the ink printability by controlling the ink rheological properties such as surface tension (27 dynes cm^{-1}), viscosity (2.5 cP), and density (1.08 g cm^{-3}) of the $CsPbBr_3$ ink. All these values are resumed into the figure of merit Z number of 12, indicating smooth jetting of inks. The calculations for Z values are mentioned in Supplementary Tables S1 and S2.

The contact angle and GFETS20 digital picture are given in Fig. 1e, f, respectively, indicating good wettability with SiO_2/Si substrate. A low-resolution SEM image of printed perovskite pattern on GFET-S20 is given in Fig. 1g, indicating clear distinction between perovskite layers and graphene blocks highlighted in yellow. The corresponding SEM images of SLG and PVK layers are given in Fig. 1h, i indicate the presence of SLG and uniform, pin-hole-free printing of continuous perovskite layers.

Graphene is integrated with perovskite in PDs primarily to leverage its exceptionally high electron mobility, which plays a critical role in enhancing charge extraction and transport. CVD graphene's intrinsic mobility often exceeds 10^4–10^5 cm^2/V s, enables rapid collection and movement of photo-generated electrons from the perovskite layer, thereby minimizing recombination losses and significantly improving responsivity and response speed[27].

The delocalized π-electron system of defect-free monolayer graphene allows for low-resistance, ballistic charge transport, while its excellent optical transparency of about 97.7% ensures minimal light absorption loss. In contrast, defective or multilayer graphene introduces trap states, increases recombination, and impedes interfacial charge transfer, ultimately degrading device performance[43]. Therefore, the structural quality of graphene is essential for maximizing the efficiency and sensitivity of perovskite–graphene hybrid PDs.

Raman spectroscopy serves as a powerful tool for assessing the quality of graphene, and it was employed to study the quality of pristine graphene from the FET chip before depositing perovskite layers, as presented in Fig. 2a. The Raman spectrum presented exhibits clear signatures of high-quality monolayer CVD graphene. A sharp and intense 2D peak around ~2700 cm^{-1}, with an $I_{(2D)}/I_G$ ratio greater than 2 confirms the monolayer nature and low strain of the graphene sheet[44]. The relatively weak D peak near ~1350 cm^{-1} indicates a low defect density, suggesting minimal structural disorder or edge imperfections in the graphene. The G peak, located around ~1580 cm^{-1}, appears at its expected position, implying negligible doping or strain effects. Notably, the 2D peak exhibits a full width at half maximum (FWHM) of approximately 35.16 cm^{-1}, and the area ratio A (2D/G) is around 3.40, as determined from Lorentzian fitting. These Raman features collectively confirm that the CVD-grown graphene is uniform, largely defect-free, and of high structural quality, suitable for applications requiring high carrier mobility, such as PDs.

The morphological characteristics of the perovskite nanocrystal ink prior to deposition are shown in Supplementary Fig. S1, revealing $CsPbBr_3$ nano-cubes with an average edge length of 10.3 ± 2.4 nm. Our previous work[42], has demonstrated that annealing temperature plays a critical role in determining the resulting crystal structure. Specifically, as the annealing temperature increases, the initially pure $CsPbBr_3$ phase tends to transform into a mixed phase comprising both $CsPbBr_3$ and Cs_4PbBr_6. Since the intended application is a broadband photodetector, it is essential that the functional ink undergoes partial conversion to the Cs_4PbBr_6 phase upon deposition, as this phase exhibits strong absorption in the UV region.

To confirm the presence of a mixed phase and separate phase, the perovskite ink was inkjet-printed and annealed at 90 °C on TEM grids for structural analysis. The TEM images (Fig. 2b) clearly reveal the coexistence of 3D $CsPbBr_3$ nano-cubes and 0D spherical Cs_4PbBr_6 particles, even at this

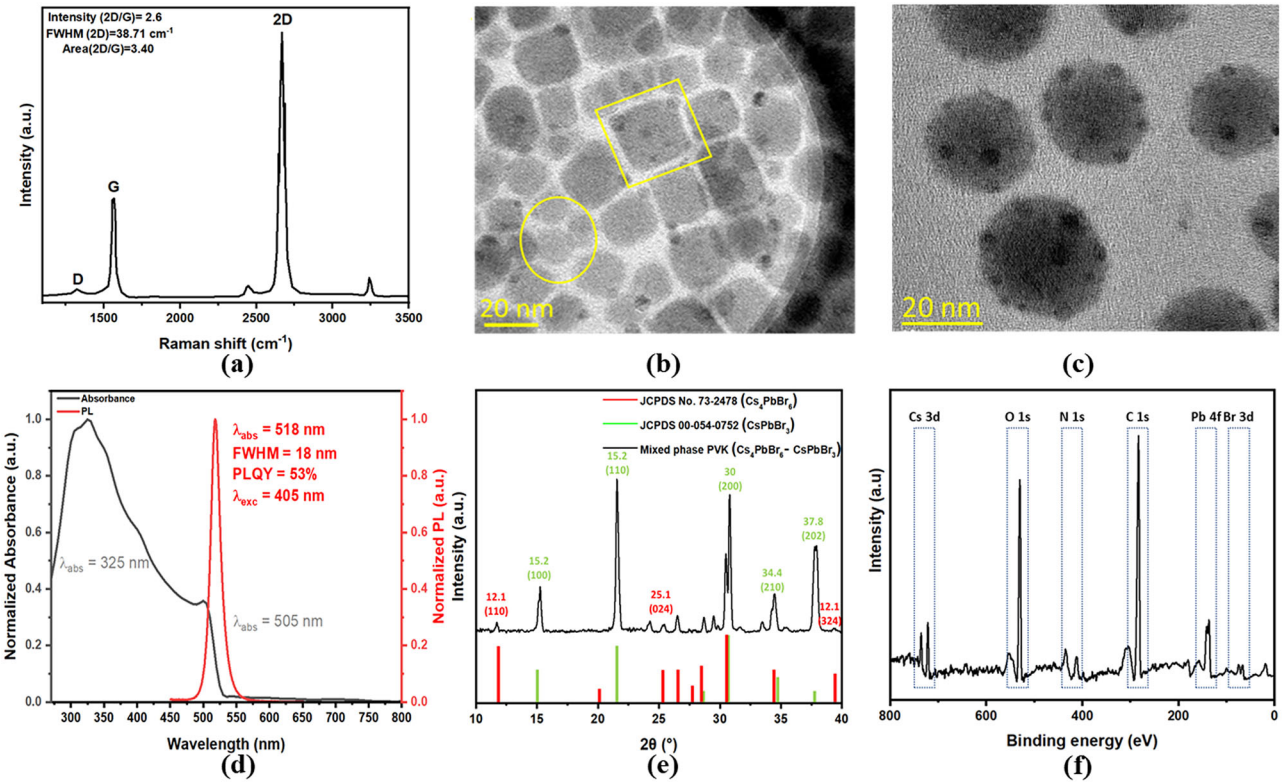

Fig. 2 | Structural, optical, and compositional characterization of the graphene–perovskite materials. a Raman spectrum of CVD graphene showing D, G, and 2D bands, confirming monolayer quality with low defect density. **b** TEM images showing nanocrystalline morphology of $CsPbBr_3$ cubic and Cs_4PbBr_6 spherical phase for the sample annealed at 90 °C. **c** TEM images showing nanocrystalline morphology of mixed phase for sample annealed at 120 °C. **d** Absorbance and PL spectra of the inkjet-printed perovskite film showing an absorption edge at 505 nm and emission peak at 518 nm **e** XRD and **f** XPS survey scan of powder dried ink.

low annealing temperature, as highlighted in yellow. Furthermore, annealing the sample at 120 °C promotes the formation of mixed phase as shown in Fig. 2c. Identical samples also annealed at 120 °C were printed on fused silica substrates for absorption measurements. Both sets of samples were annealed at the optimized temperature of 120 °C, as established in our previous study[42], to promote the formation of a mixed phase.

Furthermore, the UV–vis absorption spectrum reveals two distinct absorption features indicative of different phases. A sharp excitonic peak centered at 518 nm is characteristic of $CsPbBr_3$, suggesting the presence of well-defined perovskite NCs with strong light-harvesting capability. In contrast, a broader absorption feature centered around 325 nm is observed, which is commonly attributed to the wide-bandgap Cs_4PbBr_6 phase[45]. This high-energy absorption, which lies outside the visible range, confirms the coexistence of a secondary, non-emissive phase within the sample. These spectral features collectively indicate that the material comprises both $CsPbBr_3$ and Cs_4PbBr_6, each contributing distinct optical signatures to the absorption profile. Besides this, the PL spectrum shows a strong and narrow emission peak centered at 518 nm with a FWHM of 18 nm and a PLQY of 53%, which are consistent with the radiative recombination behavior of $CsPbBr_3$ NCs, whereas a narrow PL indicates good crystallinity and lower non-radiative losses of our inkjet printed films. Since Cs_4PbBr_6 is typically nonluminescent, the PL emission must originate exclusively from $CsPbBr_3$ domains, as discrete NCs or embedded within the Cs_4PbBr_6 matrix.

Further structural validation of this mixed-phase composition was obtained through powder X-ray diffraction (XRD) analysis, as shown in Fig. 2e. The XRD pattern displays prominent reflections at 15.2°, 21.5°, and 30.6° (2θ), corresponding to the (100), (110), and (200) planes of cubic $CsPbBr_3$, in agreement with JCPDS No. 00-054-0752. In addition, distinct peaks at 12.1°, 25.3°, and 39° (2θ) match well with the (110), (024), and (324) planes of the trigonal Cs_4PbBr_6 phase, consistent with JCPDS No. 73-2478[46]. The presence of well-defined diffraction features from both phases confirms their structural coexistence in the film and supports the interpretation drawn from the optical measurements.

Further confirmation of the surface composition and phase concentration of the dried powder ink was performed using X-ray photoelectron spectroscopy (XPS). The survey scan, shown in Fig. 2f, confirms the presence of Cs, Pb, and Br at their characteristic binding energies of approximately 724.5 eV (Cs 3d), 138.5 eV (Pb 4f), and 68.5 eV (Br 3d). To determine the relative phase composition at the surface, high-resolution scans of the Cs 3d and Pb 4f regions were recorded and analysed by peak fitting using Casa XPS software as shown in Supplementary Fig. S2. The resulting atomic Cs/Pb ratio was found to be 1.75. Since the ideal Cs/Pb ratios for pure $CsPbBr_3$ and Cs_4PbBr_6 phases are 1 and 4, respectively, this intermediate value indicates a mixture of these two phases. This ratio corresponds to an approximate composition of 64% $CsPbBr_3$ and 36% Cs_4PbBr_6 in the surface region. By tuning the $CsPbBr_3/Cs_4PbBr_6$ ratio through controlled post-deposition annealing, we can fabricate a broadband photodetector architecture. This tunability, enabled by intentional phase mixing, would not be achievable with single-phase systems and represents the most distinctive advance of our approach. It offers a clear pathway toward application-specific PDs, where spectral response can be engineered through scalable, mask-free, and vacuum-free processing strategies.

Photoluminescence quenching and carrier lifetime reduction in perovskite–graphene hybrids

Hybrid structures composed of metal halide perovskites and graphene offer a promising route to enhance photodetector performance due to their complementary optoelectronic properties. While perovskites exhibit strong absorption and long carrier diffusion lengths, graphene provides exceptional carrier mobility and conductivity. When integrated, graphene can act

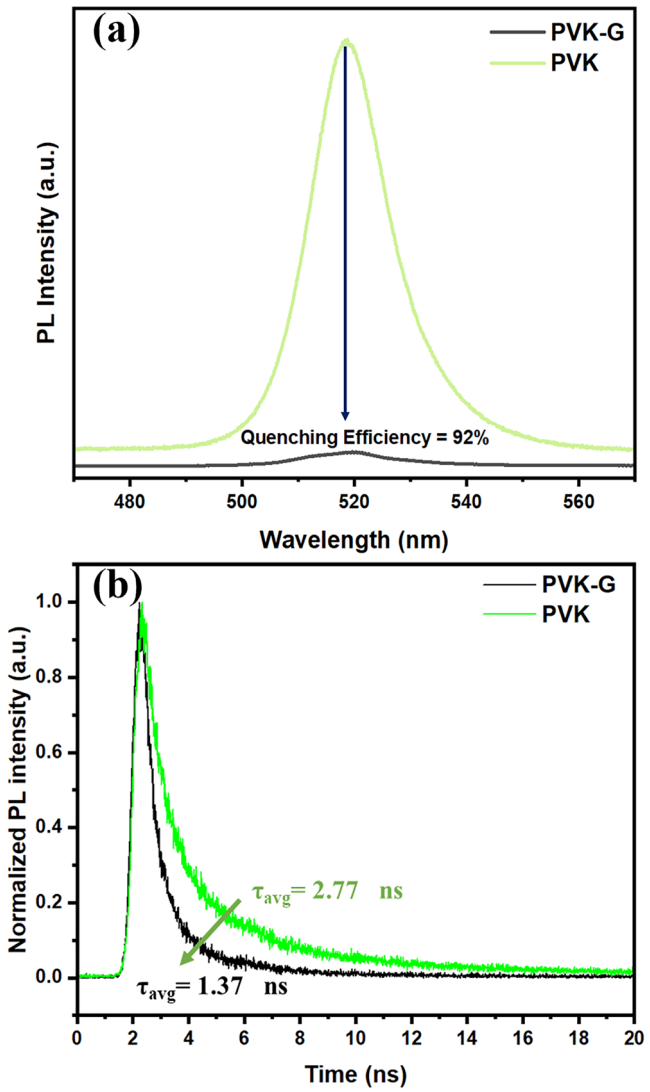

Fig. 3 | Photoluminescence characterization demonstrating charge transfer at the perovskite–graphene interface. a Photoluminescence (PL) spectra of perovskite deposited on graphene (PVK-G) and pristine perovskite (PVK) showing a strong emission peak at 518 nm. A significant quenching of 92% in the PVK-G sample indicates efficient charge transfer from perovskite to graphene. **b** Time-resolved photoluminescence (TRPL) decay curves for PVK and PVK-G samples. The PVK-G exhibits a shorter average carrier lifetime (τ_{avg} = 1.37 ns) compared to pristine PVK (τ_{avg} = 2.77 ns), confirming accelerated non-radiative recombination due to effective interfacial charge extraction by graphene.

as an efficient charge extraction layer, promoting rapid separation and transport of photogenerated carriers and thereby suppressing recombination losses. To probe the charge transfer efficiency at the perovskite–graphene interface, photoluminescence (PL) and time-resolved PL (TRPL) measurements were conducted.

Figure 3a presents the PL spectra for two configurations: perovskite deposited directly on graphene (PVK-G) and perovskite without graphene (PVK). Both samples exhibit a characteristic emission peak at 518 nm, which is attributed to the $CsPbBr_3$ phase. Notably, Cs_4PbBr_6 present in the composite, is nonluminescent due to its large band gap (4.0 eV), hence the visible excitation does not create electron–hole pairs[47].

The PL intensity of the PVK-G hybrid is significantly quenched compared to pristine PVK, with a calculated quenching efficiency of 92%, as determined using Eq. (2). This substantial reduction in radiative recombination reflects highly efficient charge transfer from the photoexcited perovskite to the underlying graphene layer[37]. The dramatic PL quenching arises from strong π–π interactions between the perovskite and the sp^2-hybridized graphene layer, which facilitate rapid and effective charge carrier transfer.

In pristine perovskite, photoexcited electron–hole pairs typically recombine within the carrier lifetime, resulting in characteristic PL emission corresponding to the bandgap energy. However, when interfaced with graphene, the photogenerated holes in the perovskite are rapidly extracted to the graphene layer, which acts as an efficient hole-transport medium due to favorable band alignment and high carrier mobility. This charge transfer reduces the density of available states for radiative recombination, thereby suppressing PL emission[38]. As a result, the photoexcited electrons in the perovskite conduction band remain trapped, unable to decay radiatively. This charge transfer mechanism underlies the pronounced PL quenching observed in the graphene–perovskite hybrid system[40,48].

$$QE\,(\%) = \frac{I_0 - I}{I_0} \times 100 \tag{2}$$

Where, QE = Quenching efficiency I_0 = Initial intensity without graphene I = Intensity with graphene

To further validate the interfacial charge transfer dynamics, TRPL measurements were performed [Fig. 3b]. The decay curves were fitted with a bi-exponential function, capturing both fast (τ_1) and slow (τ_2) recombination processes associated with non-radiative surface states and bulk radiative recombination, respectively. The pristine PVK sample displayed an average lifetime (τ_{avg}) of 2.77 ns, while PVK-G exhibited a shorter lifetime of 1.37 ns, which was calculated using Eq. (3). This pronounced reduction in carrier lifetime upon graphene integration indicates accelerated non-radiative recombination, attributed to effective carrier extraction by graphene.

$$\tau_{avg} = \frac{B_1\tau_1^{\,2} + B_2\tau_2^{\,2}}{B_1\tau_1 + B_2\tau_2} \tag{3}$$

τ_{avg} = The average fluorescence lifetime

B_1, B_2 = The pre-exponential factors (or amplitudes) obtained from fitting the fluorescence decay curve with a bi-exponential model.

τ_1, τ_2 = The fluorescence lifetimes of two distinct decay components.

The combination of PL quenching and shortened TRPL decay time provides compelling evidence for efficient interfacial charge transfer in the PVK-G hybrid system. This synergistic interaction enhances carrier dynamics and underpins the improved photodetector performance observed in graphene-integrated perovskite devices.

Further investigation was performed to find the influence of the formation of the mixed phase on the optical properties of the material; hence, PL intensity and TRPL were measured for pristine $CsPbBr_3$ and composite $CsPbBr_3$-Cs_4PbBr_6 samples, as shown in Supplementary Fig. S3. The mixed-phase film exhibits a significantly higher PL intensity and a longer average lifetime (2.76 ns) compared to the pristine $CsPbBr_3$ (1.19 ns). This improvement in the PL suggests that the formation of the $CsPbBr_3$-Cs_4PbBr_6 biphasic structure effectively passivates nonradiative defects and suppresses trap-assisted recombination, resulting in enhanced radiative efficiency. The enhanced radiative efficiency is related to the process of 'survival of the fittest' in which only stable and highly crystalline $CsPbBr_3$ are retained, whereas unstable structures get converted into Cs_4PbBr_6. These highly stable and crystalline structure can fully absorb the light, leading to significant reduction in the non-radiative recombination and florescence enhancement effect. Similar enhancement in PL intensity and TRPL lifetime increment upon Cs_4PbBr_6 conversion has been reported by Su et al.[49], where the conversion of $CsPbBr_3$ into Cs_4PbBr_6 phase was shown to reduce surface defect density and improve emission yield.

Electro-optical characterization

Preliminary evaluation of the photodetection behavior of the perovskite–graphene hybrid device was conducted with white light from the solar simulator (see Section "Characterization"), and the resulting

photocurrent was measured over time as shown in Fig. 4a at a constant voltage of 5 V. Upon illumination, the current exhibited a sharp increase from the baseline current, indicating a strong and prompt photo response. This is attributed to efficient photogeneration of charge carriers in the perovskite layer and subsequent rapid hole transfer to the graphene channel. The graphene's high carrier mobility ensures fast charge collection, resulting in a photocurrent of 243 μA, calculated using the formula given in Eq. (4).

$$I_p = I_{light} - I_{dark} \quad (4)$$

Where I_p = Photocurrent I_{light} = Current under illumination I_{dark} = Dark current

This large photocurrent enhancement strongly supports the occurrence of efficient hole transfer from perovskite to graphene, a conclusion further corroborated by PL quenching measurements, and reduced decay time from time-resolved PL measurement due to rapid carrier extraction as discussed in the previous section. The current swiftly returned to the baseline level once the light source was turned off, demonstrating excellent reversibility and minimal carrier trapping.

Based on the transient response, the rise time (10%–90%) was approximately 190 μs as shown in the inset of Fig. 4a. These results highlight the strong interfacial charge transfer dynamics and confirm the potential of the perovskite–graphene hybrid system for reliable and fast photodetection applications.

Furthermore, to assess the influence of applied bias on the photodetection performance, current–voltage (I–V) measurements were carried out under both dark and illuminated conditions, as shown in Fig. 4b. The device exhibited a linear, ohmic response, indicating good electrical contact and efficient charge transport through the perovskite–graphene hybrid interface. Upon illumination, a clear increase in current was observed, as highlighted in the inset of the Fig. 4b. This enhancement arises from the efficient light absorption in the perovskite (PVK) layer, which serves as the primary photoactive material, generating electron–hole pairs that are subsequently transferred to the graphene channel. In contrast, the device before printing perovskite also exhibited ohmic behavior, as shown in

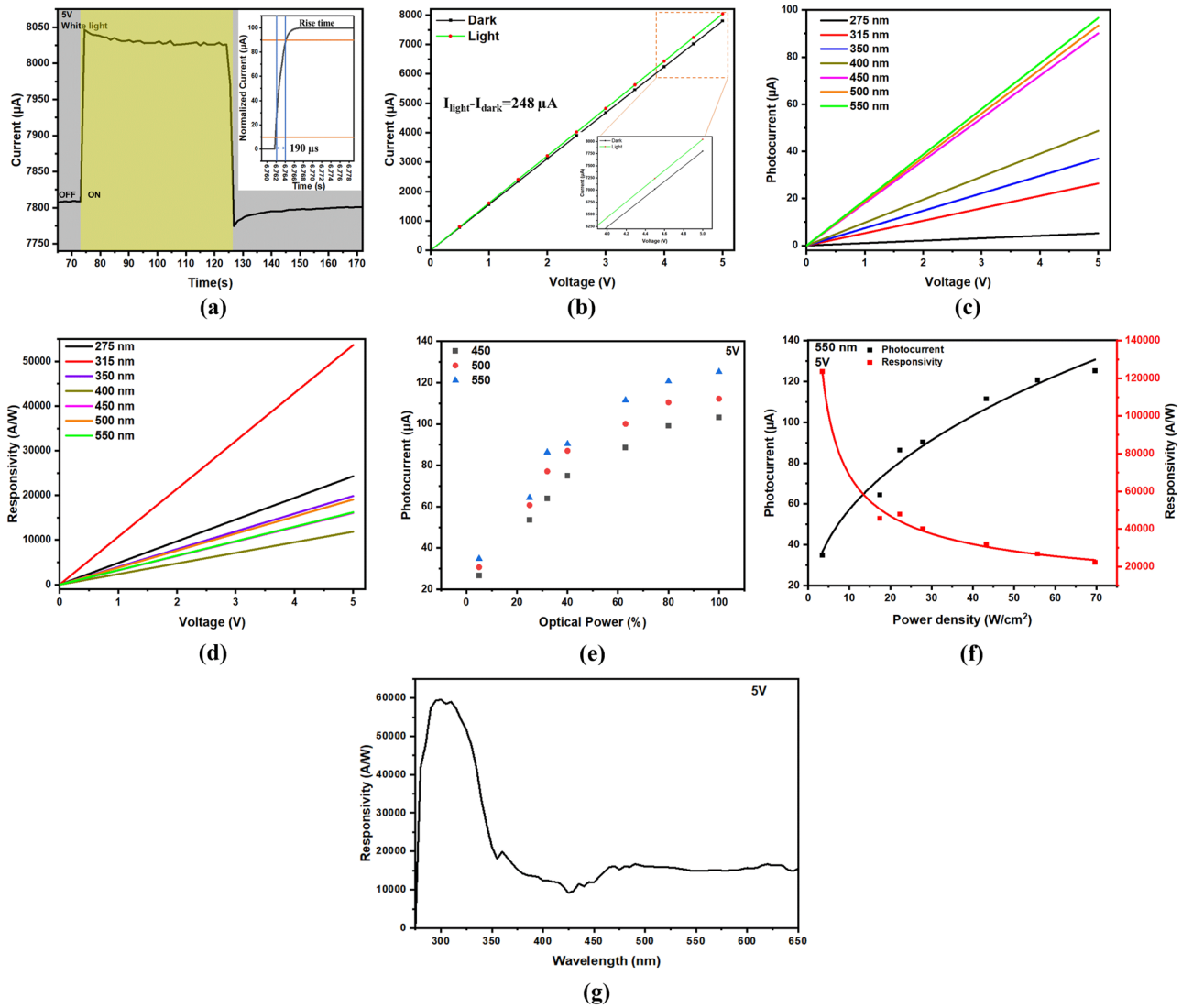

Fig. 4 | Photodetection performance of the inkjet-printed $CsPbBr_3$/ Cs_4PbBr_6 perovskite–graphene hybrid device under varying conditions. a Time-dependent photo-response under periodic white light illumination (5 V bias), demonstrating fast response and recovery. **b** I–V characteristics in dark and under illumination, confirming photocurrent generation. **c** Photocurrent variation with voltage under monochromatic light at various wavelengths (275–550 nm). **d** Responsivity versus voltage for different excitation wavelengths, showing higher responsivity in the UV region. **e** Photocurrent as a function of incident optical power at 450, 500, and 550 nm. **f** Responsivity and photocurrent trends as a function of power density (at 550 nm). **g** Spectral responsivity curve of the device measured at 5 V, showing maximum responsivity around 310 nm and broadband sensitivity across UV–visible range.

Supplementary Fig. S4, but showed no change in current under illumination, corroborating the lower absorption properties of SLG absorbs. This difference highlights the role of the printed perovskite layer in enabling photo response, confirming its function as an effective light-absorption and charge-generating layer within the device architecture.

The absorption spectrum displays a broad spectral response (ultraviolet and visible) as discussed before which is an indicative of the dual-phase nature of the material system. This broad absorption is attributed to the co-presence of $CsPbBr_3$, which absorbs efficiently in the visible region, and Cs_4PbBr_6, which contributes to absorption in the UV region due to its wider bandgap[50]. To evaluate the photodetection capability, photocurrent measurements were carried out under monochromatic illumination from 275 to 550 nm across a voltage range of 0.25–5 V as shown in Fig. 4c. A nearly linear increase in photocurrent with applied bias was observed for all wavelengths, suggesting effective charge separation and transport. The photocurrent also showed a strong dependence on wavelength, increasing progressively from 275 to 550 nm, with the highest photocurrent recorded at 550 nm. This behavior is consistent with the visible absorption of $CsPbBr_3$, indicating that it is the dominant contributor to photocurrent generation under visible light, as also confirmed by the XPS analysis.

Furthermore, applying a higher bias voltage to PD can significantly enhance the photocurrent response. This enhancement arises from the reduced carrier transit time across the photoconductive channel under stronger electric fields, which in turn increases the photoconductive gain of the device for photoconductor-based PDs. As the gain is directly proportional to the product of carrier lifetime and mobility over transit time, a higher bias facilitates more efficient carrier extraction and separation, thereby boosting the overall photocurrent. However, it is important to note that this improvement in performance is accompanied by a corresponding increase in dark current, which may compromise the signal-to-noise ratio and limit the device's detectivity under low-light conditions[28].

The responsivity (R), calculated using Eq. (5) and plotted in Fig. 4d, further highlights the spectral performance of the photodetector. Notably, the maximum responsivity was observed at 312 nm, reaching 57,245 A/W at 5 V, which aligns with the UV absorption capabilities of Cs_4PbBr_6. The lowest responsivity was recorded at 400 nm (13,358 A/W). At longer wavelengths (450–550 nm), while the responsivity decreases, the photocurrent remains significantly high, confirming efficient light harvesting and carrier generation by $CsPbBr_3$. The complementary absorption of both $CsPbBr_3$ and Cs_4PbBr_6, across UV and visible regions, enables broadband photodetection with strong voltage-dependent photo response, positioning this hybrid material as a promising candidate for optoelectronic applications, including UV–vis PDs.

The ultrahigh responsivity and strong photocurrent generation can be attributed to the photogating effect arising at the perovskite–graphene interface[51]. Upon illumination, photogenerated electrons tend to remain trapped in the $CsPbBr_3$ NCs, while the photogenerated holes are injected into the graphene. This results in hole doping of the graphene layer and a downward shift of its Fermi level. The trapped electrons act as a persistent local electrostatic gate, modulating the conductivity of the graphene channel through capacitive coupling. Because these trapped carriers exhibit long lifetimes, they continue to influence the channel current even after the light is turned off, effectively maintaining or amplifying the photocurrent beyond the initial photon absorption event. This persistent gating field, combined with the ultrahigh carrier mobility of graphene, produces a large photoconductive gain leading to enhanced responsivity and sensitivity[52].

$$R_{ext} = \frac{I_p}{P_{in}} \tag{5}$$

R_{ext} = Responsivity (A/W) I_p = Photocurrent (A), i.e., the current generated due to light exposure P_{in} = Incident optical power on the active area of the device (W).

To further investigate the device's photoresponse characteristics, the photocurrent was measured at different optical power levels for three selected wavelengths (450, 500, and 550 nm), which previously exhibited the highest photocurrent values. As shown in Fig. 4e, an increase in optical power results in a corresponding rise in photocurrent for all three wavelengths. The 550 nm illumination consistently yields the highest photocurrent, reaching over 120 μA at full optical power (100%), followed by 500 and 450 nm. This trend reflects the increased generation of photocarriers with enhanced photon flux, highlighting the efficient light absorption and charge extraction at these wavelengths. The optical power was modulated using a nondispersive lens, where 100% represents unfiltered monochromatic light.

Additionally, Fig. 4f presents the photocurrent and responsivity as functions of incident power density at 550 nm under a bias of 5 V. The photocurrent increases sub-linearly with rising power density, suggesting a photogating or trap-filling effect, where trap states become saturated at higher light intensities. In contrast, the responsivity decreases sharply with increasing power density, reaching a maximum at low intensities and gradually declining. This inverse relationship indicates that at lower light levels, the device generates higher photocurrent per unit of incident power, which is a desirable trait for low-light sensing applications.

The spectral responsivity of the device was further characterized under a constant bias of 5 V across a broad wavelength range (275–650 nm), as shown in Fig. 4g. The device exhibits a strong and broadband photo response, with a distinct peak responsivity observed around 310–312 nm, reaching values exceeding 55,000 A/W, which is higher than many commercially available PDs. This pronounced UV response can be attributed to the presence of the Cs_4PbBr_6 phase, which is known to have strong absorption in the ultraviolet region due to its wide bandgap and efficient carrier generation under UV illumination. Beyond 320 nm, the responsivity exhibits a sharp decline, followed by a relatively broad and moderate response in the visible range. Between 400–600 nm, the responsivity plateaus around 10,000–15,000 A/W, which is consistent with the absorption characteristics of $CsPbBr_3$, known to dominate the visible light region. This visible-range activity highlights the contribution of $CsPbBr_3$ NCs embedded within or in proximity to the Cs_4PbBr_6 matrix, creating a dual-phase composite responsive across both UV and visible regions. The responsivity values match well with the absorption spectra, in which there is maximum absorption peaking at the UV region and decreasing in the visible region.

The overall responsivity trend closely mirrors the absorption behavior of the material, confirming effective light harvesting and photocarrier generation across a wide spectral range. The high responsivity, particularly in the UV region, positions this material system as a strong candidate for applications in broadband photodetection, especially for UV sensing.

Although the fabricated perovskite/graphene photodetector demonstrates a very high responsivity, the ON/OFF ratio is relatively low due to the high dark current. The elevated dark current originates mainly from the intrinsic conductivity of graphene and the efficient charge transfer at the perovskite/graphene interface, which, while enhancing carrier mobility and photo response, also contributes to leakage current under dark conditions. This results in a reduced contrast between the photocurrent and dark current levels. Such a trade-off between responsivity and ON/OFF ratio is commonly observed in hybrid perovskite/graphene PDs, where the mechanisms that boost responsivity, such as photogating and trap-assisted gain, tend to increase the dark current. Similar limitations have been reported by many studies in which graphene/perovskite hybrid PDs are developed[53,54]. Nevertheless, the high responsivity achieved in our device highlights the excellent light–matter interaction and carrier transport efficiency of the perovskite/graphene interface. Future efforts should focus on suppressing dark current through interface passivation, optimized electrode design, or selective carrier blocking layers to enhance the ON/OFF ratio while retaining the high responsivity.

Further PD performance indicators, such as NEP, which represents the minimum detectable optical power per unit bandwidth and can be calculated based on Eq. (6) and specific detectivity (D^*), which is a critical figure of merit for evaluating the performance of PDs, especially when comparing devices with different active areas and noise levels were calculated. D^*

represents the photodetector's ability to detect weak optical signals over background noise and is typically expressed in Jones (cm $Hz^{(1/2)}$ W^{-1}). A higher D^* value indicates better sensitivity and lower noise floor. It is calculated using Eq. (7) in cases where the dark currents or shot noise current are the major contributor to the noise[55,56].

$$NEP = \frac{i_n}{R_{ext}} = \frac{\sqrt{2qI_{d(SLG)}}}{R_{ext}} \quad (6)$$

$$D^* = \frac{\sqrt{AB}}{NEP} = \frac{R_{ext}.\sqrt{AB}}{\sqrt{2qI_{d(SLG)}}} \quad (7)$$

NEP is the noise equivalent power (W $Hz^{-1/2}$)D^* is specific detectivity in Jones (cm $Hz^{1/2}$ W) R_{ext} is the responsivity (A/W) at 312 nm, A is the effective area of the device (cm^2), B is the bandwidth (Hz)q is the elementary charge (1.6×10^{-19} C), I_d is the dark current (A) of SLG.i_n is the shot noise current ($\sqrt{2qI_{d(SLG)}}$).

The calculated D^* value is 1.03×10^{16} Jones at 312 nm, which is notably higher than many conventional solution-processed PDs and demonstrates strong performance comparable to commercial silicon-based photodiodes at 312 nm[57]. The NEP was calculated to be 8.74×10^{-16} W $Hz^{1/2}$ at the same wavelength. This extremely low NEP value further confirms the device's exceptional sensitivity, making it highly suitable for practical applications in UV–vis optoelectronics and low-intensity light sensing technologies. The wavelength dependence of the specific detectivity of the device was evaluated in the 280–650 nm range (Supplementary Fig. S5). The device exhibits a peak detectivity corresponding to the UV absorption region of the perovskite active layer. As the wavelength increases beyond 350 nm, and then remains relatively constant in the visible range up to 650 nm. This trend indicates that the photodetector is highly sensitive to UV light, while its performance in the visible region is moderate but stable, consistent with the absorption characteristics of the $CsPbBr_3$-Cs_4PbBr_6 hybrid perovskite.

Stability, reliability and long-term exposure studies

In optoelectronic and photodetector systems, reliability, stability, and long-term exposure tolerance are essential parameters that govern the practical applicability of the device in real-world scenarios. Devices intended for continuous monitoring, wearable systems, or environmental sensing must exhibit consistent performance under ambient conditions, repetitive usage, and prolonged illumination. Perovskite-based optical devices typically suffer from poor stability and reliability, which severely limits their practical application. However, our raisin-bread device architecture is specifically designed to overcome these limitations, offering enhanced long-term operational stability and improved device reliability. A comprehensive testing of long-term stability, cycling reliability, and sustained operational endurance is imperative to validate material robustness and device integrity. Figure 5 illustrates the systematic evaluation of the photodetector's performance under varying reliability and stability conditions.

Long-term stability, as shown in Fig. 5a, was evaluated over a 6-month period. Devices were measured under a constant bias of 5 V and white light illumination, then stored under ambient air conditions without encapsulation. Subsequent measurements were performed monthly, revealing that the photocurrent remained nearly constant at ~250 μA throughout the entire duration. This demonstrates excellent environmental stability of the photoactive layer and consistent interfacial properties over time, an essential requirement for real-world device reliability. This remarkable stability is attributed to the unique "raisin bread" architecture, where $CsPbBr_3$ NCs are embedded within a Cs_4PbBr_6 matrix as shown in the inset of Fig. 5a.

The remarkable 6-month air stability of the $CsPbBr_3$-Cs_4PbBr_6 photodetector originates from the multifunctional protective role of the Cs_4PbBr_6 matrix. Structurally, Cs_4PbBr_6 possesses a zero-dimensional crystal framework in which isolated $[PbBr_6]^{4-}$ octahedra are fully surrounded by Cs^+ ions, forming a chemically inert and hydrophobic host[58]. When the photoactive $CsPbBr_3$ NCs ("raisins") are embedded within this dense Cs_4PbBr_6 matrix ("bread"), the matrix acts as an impermeable barrier that suppresses the diffusion of moisture and oxygen, thereby preventing hydrolysis and oxidation of the perovskite lattice[59]. At the interface, the Cs-rich environment of Cs_4PbBr_6 passivates under-coordinated Pb^{2+} and Br^{-1} sites, reducing surface trap states and non-radiative recombination. Furthermore, the discontinuous 0D connectivity of Cs_4PbBr_6 inhibits halide-ion migration between neighboring $CsPbBr_3$ grains, suppressing electrochemical degradation and phase segregation[50]. The two phases exhibit a small lattice mismatch, which relieves interfacial strain and stabilizes the cubic $CsPbBr_3$ phase under thermal and humidity cycling. The wide bandgap (~3.9 eV) and insulating nature of Cs_4PbBr_6 further confine charge carriers within $CsPbBr_3$, reducing leakage and Joule heating. Collectively, these structural, chemical, and electronic effects endow the composite with exceptional resistance to moisture-induced decomposition, enabling consistent photo-response and optical integrity after prolonged ambient exposure. This hybrid "raisin-bread" architecture thus offers a simple yet highly effective pathway toward intrinsically stable all-inorganic perovskite optoelectronic devices[60].

To evaluate cycling stability, the device was subjected to repeated on/off light switching cycles under a 5 V bias (Fig. 5b). The photocurrent demonstrated sharp, reproducible transitions between the illuminated and dark states over 10 cycles, with no noticeable baseline drift or response degradation. This behavior confirms the excellent repeatability and photo response reliability, essential for PDs requiring real-time switching and consistent output.

Figure 5c presents the photocurrent behavior under continuous light exposure for 10 min at 5 V. While a slight decay in the photocurrent was observed, the device retained approximately 82% of its initial photocurrent after 10 min. A longer duration of 1 h is shown in Supplementary Fig. S6. The high retention underscores the device's strong operational stability and endurance under constant optical stimulation.

Taken together, these results provide compelling evidence of the device's robustness across multiple reliability metrics. The photodetector exhibits stable performance under prolonged operation, repeated cycling, and extended light exposure, underscoring its suitability for integration into flexible, wearable, and portable optoelectronic platforms. Table 2 presents a comparison between our inkjet-printed photodetector and other recently reported devices. It is evident that our device outperforms many in terms of responsivity, specific detectivity, long-term stability, and NEP, highlighting its potential for advanced broad-band photodetection applications.

Conclusion

We have successfully developed a high-performance, broadband photodetector by integrating mixed-phase perovskite ($CsPbBr_3$/Cs_4PbBr_6) films with SLG on a CVD-grown FET platform, using a fully inkjet-printed fabrication process. The hybrid architecture addresses two major limitations of conventional perovskite PDs, limited charge carrier mobility and poor environmental stability by harnessing the exceptional transport properties of graphene and the enhanced robustness of the mixed-phase perovskite. Our device exhibits outstanding responsivity exceeding 57,000 A/W at 312 nm without the need for external gating, as well as a broad and stable spectral response across 270–650 nm and an excellent detectivity of 1.03×10^{16} Jones. The device demonstrated stable performance over 6 months under ambient conditions without any need for encapsulation, indicating strong inherent stability with potential for long-term operation. Additionally, the inkjet printing technique provides a scalable, cost-effective, and eco-friendly route compatible with flexible substrates and large-area electronics. These results pave the way for the next generation of inkjet-printed optoelectronic devices and offer a promising solution for applications in wearable technologies, artificial vision, and portable environmental sensing.

Materials

All chemicals, materials, and solvents used in the synthesis of $CsPbBr_3$ NCs were utilized as received from their respective suppliers, without any

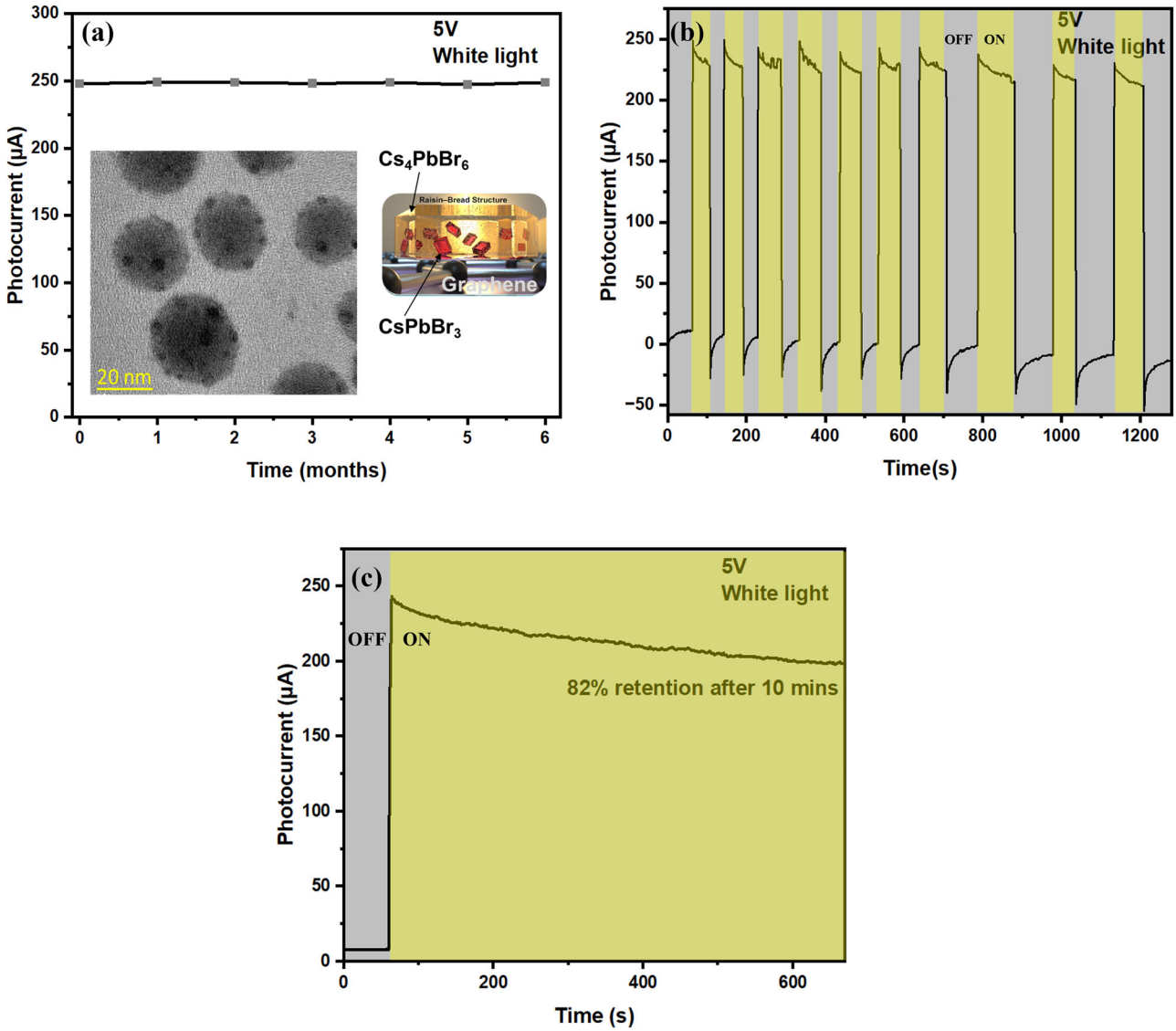

Fig. 5 | Reliability and stability performance of the photodetector under white light illumination. a Long-term stability over 6 months showing negligible degradation in photocurrent (~250 μA). Inset: TEM image illustrating the "raisin bread" perovskite structure. **b** Reproducible and stable photo response over multiple on/off illumination cycles, indicating excellent operational reliability. **c** Continuous light exposure test showing 82% photocurrent retention after 10 min, demonstrating good long-term operational stability.

Table 2 | Summary of inkjet printed perovskite photo-detectors

Sr. no	Materials	Responsivity (A/W)	Detectivity (Jones)	Long term stability	Spectral range (nm)	Reference
1	Graphene/$CH_3NH_3PbI_{3-x}Cl_x$	0.60	3.4×10^{10}	–	400–700	63
2	ITO/$CH_3NH_3PbI_3$	1.2	2.39×10^{12}	–	–	64
3	$(CH_3(CH_2)_3NH_3)_2(CH_3NH_3)_{n-1}Pb_nI_{3n+1}$	0.17	3.7×10^{12}	–	600–750	65
4	$(CH_3(CH_2)_3NH_3)_2(CH_3NH_3)_{n-1}Pb_nI_{3n+1}$	0.02	2.4×10^{11}	–	–	66
5	SLG/$CsPbBr_3$	7000	–	2 weeks	–	67
6	$MAPbI_3$	1.03	–	–	–	68
7	**SLG/$CsPbBr_3$-Cs_4PbBr_6**	**57,000**	**1.03×10^{16}**	**> 6 months**	**270–650**	**This work**

Bold highlights the main results of this work.

additional purification. The precursors included lead (II) bromide ($PbBr_2$, ABCR, 99.999%) and cesium carbonate (Cs_2CO_3, Sigma-Aldrich, 99.995%). Solvents and ligands, such as 1-octadecene (1-ODE, Sigma-Aldrich, 90%), oleic acid (OA, Sigma-Aldrich, 90%), oleylamine (OLA, Sigma-Aldrich, 90%), hexane (Hx, Sigma-Aldrich, 99%), dodecane (Sigma-Aldrich, anhydrous ≥99%), and methyl acetate (MeOAc, Sigma-Aldrich, 99.5%) were also used as received. CVD graphene FET-S20 chips were purchased from Graphenea and used as the platform for device fabrication without any further modification. These chips consist of 12 individual graphene field-effect transistors (FETs) fabricated on a single substrate, each incorporating

CVD-grown monolayer graphene patterned into a 90 × 90 μm square on a highly doped Si/SiO_2 wafer with a 285 nm oxide layer, which also serves as the global back gate. The source and drain electrodes were pre-patterned with gold, allowing direct electrical characterization of the graphene channel. According to the manufacturer's specifications, the graphene exhibits a field-effect mobility exceeding 1000 $cm^2 V^{-1} s^{-1}$, determined under back-gated operation using two-probe I–V measurements at room temperature (25 ± 2 °C) in ambient air. The devices typically show Dirac points below 25 V, consistent with high-quality CVD graphene on SiO_2.

Methods

Synthesis of perovskite ink

$CsPbBr_3$ NCs were synthesized via a modified hot-injection method adapted from Protesescu et al.[61], following procedures established in our previous work[62]. For Cs-oleate preparation, Cs_2CO_3 (0.41 g), oleic acid (1.5 mL), and 1-ODE (20 mL) were degassed at 120 °C for 1 h and then heated to 150 °C under nitrogen until complete dissolution. Separately, $PbBr_2$ (0.85 g) was dissolved in 1-ODE (50 mL), degassed at 120 °C, and mixed with a preheated OA/OLA (1:1, 10 mL) solution under nitrogen. The mixture was heated to 170 °C, followed by the injection of 4 mL Cs-oleate. After 5 s, the reaction was quenched in an ice bath. NCs were purified by sequential centrifugation and redispersion using hexane and methyl acetate, followed by overnight cold storage at −18 °C and filtration. The resulting solid was dried under nitrogen, placed under vacuum for 15 min, weighed, and redispersed in hexane or dodecane at the desired concentration, then filtered through a 0.42 μm Teflon filter.

Inkjet printing

The ink preparation followed our established methodology[42]. Two colloidal solutions of $CsPbBr_3$ NCs, dispersed in dodecane and hexane, respectively, were mixed in a 3:1 volume ratio (dodecane:hexane) and adjusted to a 10 wt % NC concentration. The mixture was vortexed for 3 min at room temperature to obtain a homogeneous perovskite NC ink.

Inkjet printing was performed using a Dimatix DMP-2831 piezoelectric drop-on-demand printer (Fujifilm Dimatix Inc.) with a Samba cartridge (12 nozzles, 2.4 pL drop volume, 20 μm drop spacing) at room temperature and ambient conditions. FETS20 chips were used as a substrate to deposit perovskite ink on SLG. Ink rheological properties, viscosity, and surface tension were optimized to ensure smooth and uniform deposition, as described in our previous works[42].

Different perovskite layers were printed in the sequence of 2 layers up to 16 layers to optimize the photocurrent. The samples were optimized, and PVK layers of 14 layers was selected for all optoelectronic measurements. Annealing was performed at 120 °C for 20 min to form $CsPbBr_3$ embedded in the Cs_4PbBr_6 matrix based on our previous study. All annealing were performed under vacuum conditions.

Characterization

Scanning electron microscopy was performed using a FEGSEM–JEOL 3100F system to examine surface morphology. Transmission electron microscopy (TEM) was conducted on a JEM-2010F TEM/STEM (JEOL Ltd., Japan) operated at 200 kV. The sample preparation involved printing 2 layers of perovskite layers on TEM carbon grid, followed by annealing at 90 °C for 10 min to confirm the presence of 2 phase. Furthermore, the Cs_4PbBr_6 matrix embedded with $CsPbBr_3$ raisin bread structure were confirmed following the same protocol but annealing at 120 °C for 20 min in order to see the phases clearly based on our previous report.

XRD measurements were performed using a Japan Rigaku D/Max-IIA diffractometer with Cu Kα radiation (λ = 1.5406 Å) at 40 kV and 40 mA to determine crystalline structure and orientation. The chemical composition and local environment of the printed perovskite NC layers were examined via XPS using a PHI ESCA-5500 spectrometer with monochromatic Al Kα radiation (E = 1486 eV) at 350.0 W. The X-ray source and detector positioned at 45.1° angle relative to the sample normal.

PL spectroscopy was conducted using a 325-nm He–Cd laser (power density: 50 mW, spot size: ~80 μm). Emission was analysed using a single-grating monochromator coupled to a GaAs photomultiplier. PL spectra were collected from three different spots per sample.

UV–vis absorption spectra of colloidal NCs were measured using a JASCO V-780 UV–vis/NIR spectrophotometer, equipped with a dual-grating monochromator and a PMT detector for the UV–vis range. Absolute PLQY was measured using a C9920-02 system with an integrating sphere and excitation at 405 nm. For measurements under illumination, the devices were exposed either to a white light source (quartz-halogen lamp) or to a combination of quartz-halogen and xenon (Xe) lamps coupled to a monochromator with a 2-nm spectral resolution, enabling monochromatic excitation. The white light provided a power density of approximately 1 kW/m^2, simulating solar irradiation (class B solar simulator). In contrast, the power density of the monochromatic illumination across the 270–1100 nm wavelength range was in the range of ~0.4–1.2 mW/m^2. Optoelectronic measurements were carried out both in the dark and under illumination using an Agilent B1500A semiconductor device analyzer. To obtain high-resolution response time measurements of the photodetector, we employed the Analog Discovery Pro (ADP3450/ADP3250), a high-performance mixed-signal oscilloscope and instrumentation device developed by Digilent. This system enables precise acquisition and analysis of fast analog signal transients, making it well-suited for capturing rapid photo response behavior.

The lamp output optical power at the device plane was calibrated using a NIST-traceable Si photodiode from Thorlabs (DET210/M), applying its manufacturer-supplied spectral responsivity to obtain the spectral irradiance at 312 nm. As an independent cross-check, we measured the optical power at the same sample position with a calibrated Thorlabs power meter (PM100A with its matched sensor head), finding consistent values within the expected instrumental uncertainty. Both calibrations were performed at the sample plane, using the same beam path as during electrical measurements. For the stability tests, the samples were stored under ambient laboratory conditions, where the relative humidity was maintained at 65% and the temperature at 20 °C. The samples were not exposed to artificial light or UV radiation throughout the 6-month storage period.

Data availability

The data that support the findings of this study are available from the corresponding authors upon reasonable request.

Received: 17 August 2025; Accepted: 31 December 2025;
Published online: 08 January 2026

References

1. Xu, R., Chin, X. Y., White, L. R. W., Mhaisalkar, S. G. & Bruno, A. Transforming near-infrared photodetectors with perovskites: materials, strategies, and future outlook. *Energy Fuels* **39**, 10744–10767 (2025).
2. Chen, S. & Shi, G. Two-dimensional materials for halide perovskite-based optoelectronic devices. *Adv. Mater.* **29**, 1605448 (2017).
3. Dong, Y. et al. Improving all-inorganic perovskite photodetectors by preferred orientation and plasmonic effect. *Small* **12**, 5622–5632 (2016).
4. Shen, Y. et al. Two-dimensional $CsPbBr_3$/PCBM heterojunctions for sensitive, fast and flexible photodetectors boosted by charge transfer. *Nanotechnology* **29**, 085201 (2018).
5. Gu, L. et al. 3D arrays of 1024-pixel image sensors based on lead halide perovskite nanowires. *Adv. Mater.* **28**, 9713–9721 (2016).
6. Deng, W. et al. Aligned single-crystalline perovskite microwire arrays for high-performance flexible image sensors with long-term stability. *Adv. Mater.* **28**, 2201–2208 (2016).
7. Lee, M. et al. An amphibious artificial vision system with a panoramic visual field. *Nat. Electron.* **5**, 452–459 (2022).

8. Li, Z., Yan, T. & Fang, X. Low-dimensional wide-bandgap semiconductors for UV photodetectors. *Nat. Rev. Mater.* **8**, 587–603 (2023).
9. Jin, H. et al. Phase stabilization of cesium lead iodide perovskites for use in efficient optoelectronic devices. *NPG Asia Mater.* **16**, 1–18 (2024).
10. Vescio, G. et al. High quality inkjet printed-emissive nanocrystalline perovskite $CsPbBr_3$ layers for color conversion layer and LEDs applications. *Adv. Mater. Technol.* **7**, 2101525 (2022).
11. Adl, H. P. et al. Tailoring single-mode random lasing of Tin halide perovskites integrated in a vertical cavity. *Adv. Mater.* **36**, 2313252 (2024).
12. Kim, M. et al. An aquatic-vision-inspired camera based on a monocentric lens and a silicon nanorod photodiode array. *Nat. Electron.* **5**, 478–478 (2022).
13. Gu, L. et al. A biomimetic eye with a hemispherical perovskite nanowire array retina. *Nature* **581**, 278–282 (2020).
14. Bai, W. et al. Bioresorbable photonic devices for the spectroscopic characterization of physiological status and neural activity. *Nat. Biomed. Eng.* **3**, 644–654 (2019).
15. Yokota, T. et al. A conformable imager for biometric authentication and vital sign measurement. *Nat. Electron.* **3**, 113–121 (2020).
16. Li, B. et al. Surface passivation engineering strategy to fully-inorganic cubic $CsPbI_3$ perovskites for high-performance solar cells. *Nat. Commun.* **9**, 1–8 (2018).
17. Dou, L. et al. Solution-processed hybrid perovskite photodetectors with high detectivity. *Nat. Commun.* **5**, 1–6 (2014).
18. Stranks, S. D. et al. Electron-hole diffusion lengths exceeding 1 micrometer in an organometal trihalide perovskite absorber. *Science* **342**, 341–344 (2013).
19. Yu, J. et al. Perovskite $CsPbBr_3$ crystals: growth and applications. *J. Mater. Chem. C* **8**, 6326–6341 (2020).
20. Ullah, S. et al. All-inorganic $CsPbBr_3$perovskite: a promising choice for photovoltaics. *Mater. Adv.* **2**, 646–683 (2021).
21. Khan, J. et al. Eco-friendly alkali lignin-assisted water-based graphene oxide ink and its application as a resistive temperature sensor. *Nanotechnology* **35**, 055301 (2024).
22. Htwe, Y. Z. N., Mariatti, M. & Khan, J. Review on solvent-and surfactant-assisted water-based conductive inks for printed flexible electronics applications. *J. Mater. Sci. Mater. Electron.* **35**, 1191 (2024).
23. Khan, J., Weis, M. & Mariatti, M. Inkjet-printed temperature sensor from eco-friendly edge-oxidized graphene oxide ink on biodegradable polyvinyl alcohol substrate. *IEEE Sens. Lett.* **8**, 1–4 (2024).
24. Kamarudin, S. F., Abdul Aziz, N. H., Lee, H. W., Jaafar, M. & Sulaiman, S. Inkjet printing optimization: toward realization of high-resolution printed electronics. *Adv. Mater. Technol.* **9**, 2301875 (2024).
25. Arrese, J. et al. Flexible hybrid circuit fully inkjet-printed: surface mount devices assembled by silver nanoparticles-based inkjet ink. *J. Appl. Phys*. **121**, https://doi.org/10.1063/1.4977961 (2017).
26. Khan, J. et al. Flexible and highly selective NO_2 gas sensor based on direct-ink-writing of eco-friendly graphene oxide for smart wearable application. *Chemosphere* **367**, 143618 (2024).
27. Akhavan, S. et al. Graphene-perovskite fibre photodetectors. *Adv. Mater.* **36**, https://doi.org/10.1002/adma.202400703 (2024).
28. Chen, J., Jing, Q., Xu, F., Lu, Z. & Lu, Y. High-sensitivity optical-fiber-compatible photodetector with an integrated $CsPbBr_3$–graphene hybrid structure. *Optica* **4**, 835 (2017).
29. Khan, J. & Mariatti, M. In-situ graphene oxide reduction via inkjet printing using natural reducing inks. *Flex. Print. Electron.* **8**, 035009 (2023).
30. Motta, C., El-Mellouhi, F. & Sanvito, S. Charge carrier mobility in hybrid halide perovskites. *Sci. Rep.* **5**, 12746 (2015).
31. Tailor, N. K. et al. The effect of dimensionality on the charge carrier mobility of halide perovskites. *J. Mater. Chem. A* **9**, 21551–21575 (2021).
32. Thodkar, K. & Gramm, F. Enhanced mobility in suspended chemical vapor-deposited graphene field-effect devices in ambient conditions. *ACS Appl. Mater. Interfaces* **15**, 37756–37763 (2023).
33. Khan, J., Momin, S. A. & Mariatti, M. A review on advanced carbon-based thermal interface materials for electronic devices. *Carbon* **168**, 65–112 (2020).
34. Novoselov, K. S. et al. Electric field effect in atomically thin carbon films. *Science* **306**, 666–669 (2004).
35. Khan, J. & Jaafar, M. Reduction efficiencies of natural substances for reduced graphene oxide synthesis. *J. Mater. Sci.* **56**, 18477–18492 (2021).
36. Suragtkhuu, S. et al. Graphene-like monoelemental 2D materials for perovskite solar cells. *Adv. Energy Mater.* **13**, 2204074 (2023).
37. Malik, S. et al. Spray-lithography of hybrid graphene-perovskite paper-based photodetectors for sustainable electronics. *Nanotechnology* **35**, 325301 (2024).
38. Lee, Y. et al. High-performance perovskite-graphene hybrid photodetector. *Adv. Mater.* **27**, 41–46 (2015).
39. Sun, J. et al. Perovskite-graphene heterostructure biosensor integrated with biotunable nanoplasmonic ternary logic gate for ultrasensitive cytokine detection. *Adv. Sci.* e03124 https://doi.org/10.1002/advs.202503124 (2025).
40. Zhu, Z. et al. Efficiency enhancement of perovskite solar cells through fast electron extraction: the role of graphene quantum dots. *J. Am. Chem. Soc.* **136**, 3760–3763 (2014).
41. Fanizza, E. et al. $CsPbBr_3$ nanocrystals-based polymer nanocomposite films: effect of polymer on spectroscopic properties and moisture tolerance. *Energies* **13**, 6730 (2020).
42. Khan, J. et al. Effect of annealing temperature on the properties of $CsPbBr_3$ nanocrystal films via inkjet printing and its application in colour conversion layers. *Nanoscale* **17**, 17803–17815 (2025).
43. Yao, Y. et al. Controlled growth of multilayer, few-layer, and single-layer graphene on metal substrates. *J. Phys. Chem. C* **115**, 5232–5238 (2011).
44. Ferrari, A. C. et al. Raman spectrum of graphene and graphene layers. *Phys. Rev. Lett.* **97**, 187401 (2006).
45. Goswami, C. & Bhardwaj, A. Emergence of multi-peak emission in CsBr-Cs_4PbBr_6-$CsPbBr_3$ nanocrystals at room temperature. *J. Mater. Res.* **39**, 2142–2151 (2024).
46. Li, X. et al. High-performance $CsPbBr_3$@$Cs4PbBr_6$/SiO_2 nanocrystals via double coating layers for white light emission and visible light communication. *EScience* **2**, 646–654 (2022).
47. Yu, X. et al. Cs_4PbX_6 (X = Cl, Br, I) nanocrystals: preparation, water-triggered transformation behavior, and anti-counterfeiting application. *Langmuir* **34**, 10363–10370 (2018).
48. Wang, J. T. W. et al. Low-temperature processed electron collection layers of graphene/TiO 2 nanocomposites in thin film perovskite solar cells. *Nano Lett.* **14**, 724–730 (2014).
49. Su, Y. et al. Highly efficient $CsPbBr_3$ perovskite nanocrystals induced by structure transformation between $CsPbBr_3$ and Cs_4PbBr_6 phases. *J. Mater. Chem. C* **7**, 7548–7553 (2019).
50. Bai, T. et al. High stability and strong luminescence $CsPbBr_3$-Cs_4PbBr_6 thin films for all-inorganic perovskite light-emitting diodes. *RSC Adv.* **13**, 24413–24422 (2023).
51. Dirin, D. N. et al. Microcarrier-assisted inorganic shelling of lead halide perovskite nanocrystals. *ACS Nano* **13**, 11642–11652 (2019).
52. Chang, P. H. et al. Ultrahigh responsivity and detectivity graphene-perovskite hybrid phototransistors by sequential vapor deposition. *Sci. Rep.* **7**, 1–10 (2017).
53. Abbas, K. et al. Graphene photodetectors integrated with silicon and perovskite quantum dots. *Microsyst. Nanoeng.* **10**, https://doi.org/10.1038/s41378-024-00722-4 (2024).
54. Rogalski, A., Hu, W., Wang, F., Wang, Y. & Martyniuk, P. Perovskite versus standard photodetectors. *Materials* **17**, 4029 (2024).
55. Gong, X. et al. High-detectivity polymer photodetectors with spectral response from 300 nm to 1450 nm. *Science* **325**, 1665–1667 (2009).

56. Akhavan, S. et al. Graphene-black phosphorus printed photodetectors. *2D Mater.* **10**, 035015 (2023).
57. Buscema, M. et al. Photocurrent generation with two-dimensional van der Waals semiconductors. *Chem. Soc. Rev.* **44**, 3691–3718 (2015).
58. Ma, Z. et al. Pressure-induced emission of cesium lead halide perovskite nanocrystals. *Nat. Commun.* **9**, 1–8 (2018).
59. Wang, Z. et al. High stability and strong luminescence $CsPbBr_3$/Cs_4PbBr_6 perovskite nanocomposite: large-scale synthesis, reversible luminescence, and anti-counterfeiting application. *Adv. Mater. Technol.* **6**, 2100654 (2021).
60. Sun, W., Hung, Y. T., Huang, W. T., Liu, R. S. & Zhou, W. Photoluminescent nano-$CsPbBr_3$ embedded in Cs_4PbBr_6 crystals: formation mechanism and properties. *Cryst. Growth Des.* **24**, 545–553 (2024).
61. Protesescu, L. et al. Nanocrystals of cesium lead halide perovskites ($CsPbX_3$, X = Cl, Br, and I): novel optoelectronic materials showing bright emission with wide color gamut. *Nano Lett.* **15**, 3692–3696 (2015).
62. Vescio, G. et al. Fully inkjet-printed green-emitting PEDOT:PSS/NiO/colloidal $CsPbBr_3$/SnO_2 perovskite light-emitting diode on rigid and flexible substrates. *Adv. Eng. Mater.* **25**, 2300927 (2023).
63. Alamri, A. M., Leung, S., Vaseem, M., Shamim, A. & He, J. H. Fully inkjet-printed photodetector using a graphene/perovskite/graphene heterostructure. *IEEE Trans. Electron Devices* **66**, 2657–2661 (2019).
64. Liu, Y. et al. Inkjet-printed photodetector arrays based on hybrid perovskite $CH_3NH_3PbI_3$ microwires. *ACS Appl. Mater. Interfaces* **9**, 11662–11668 (2017).
65. Min, M., Hossain, R. F., Adhikari, N. & Kaul, A. B. Inkjet-printed organohalide 2d layered perovskites for high-speed photodetectors on flexible polyimide substrates. *ACS Appl. Mater. Interfaces* **12**, 10809–10819 (2020).
66. Min, M., Hossain, R. F., Ma, L.-C. & Kaul, A. B. Fabrication and characterization of inkjet-printed 2D perovskite optoelectronic devices. *J. Vaccum Sci. Technol. A* **38**, 52202 (2020).
67. Austin, J. S. et al. Photosensitisation of inkjet printed graphene with stable all-inorganic perovskite nanocrystals. *Nanoscale* **15**, 2134–2142 (2023).
68. Gu, Z. et al. Controllable printing of large-scale compact perovskite films for flexible photodetectors. *Nano Res.* **15**, 1547–1553 (2022).

Acknowledgements

This work was funded by the Ministry of Science and Innovation of Spain under the projects LIP-FREE (PID2022-140978OB-I00) and PIXIE-SENS (PDC2023-145804-I00). This work has been partially supported by the PROMETEO Program from the Generalitat Valenciana (Q-solutions project reference CIPROM/2021/078). Junaid Khan and J.Marí-Guaita acknowledges the financial backing from grant JDC2024-054497-I and JDC2022-049260-I, respectively funded by the Spanish Ministry of Science and Innovation and by the European Union Next Generation EU/PRTR. This work was also supported by the EU Next Generation through the Recovery and Resilience Plan for Slovakia under the project No. 09I05-03-V02-00030, Research of fabrication technology for low-cost oxide-based semiconductor electronic devices for IoT and sensor applications.

Author contributions

Junaid Khan conceived and designed the study, performed the experiments, analysed the data, and wrote the original draft of the manuscript. Júlia Marí-Guaita, Joshua D. Forero, and Kenneth Lobo assisted in performing experiments. Francisco Palacio, Giovanni Vescio and Sergi Hernández contributed to optical measurements. Raúl I. Sánchez and Juan P. Martínez carried out the time-resolved photoluminescence (TRPL) measurements. Iván Mora-Seró and Carina Pareja-Rivera synthesized the perovskite inks. Martin Weis, Albert Cirera, Sergi Hernández, and Blas Garrido provided funding support, supervised the project, and helped with manuscript review and editing. All authors discussed the results and contributed to the final version of the manuscript.

Competing interests

The authors declare no competing interests.

Additional information

Supplementary information The online version contains supplementary material available at https://doi.org/10.1038/s43246-025-01071-z.

Correspondence and requests for materials should be addressed to Junaid Khan.

Peer review information *Communications Materials* thanks Rajesh Kumar Ulaganathan and the other anonymous reviewer(s) for their contribution to the peer review of this work. A peer review file is available.